Journal of Catalysis 360 (2018) 152–159

Contents lists available at ScienceDirect

Journal of Catalysis

journal homepage: www.elsevier.com/locate/jcat

Effects of zeolite particle size and internal grain boundaries on Pt/Beta catalyzed isomerization of *n*-pentane

Guanghua Ye [a], Yuanyuan Sun [a], Zhongyuan Guo [a], Kake Zhu [a], Honglai Liu [a], Xinggui Zhou [a,*], Marc-Olivier Coppens [b,*]

[a] State Key Laboratory of Chemical Engineering, East China University of Science and Technology, Shanghai 200237, China
[b] Department of Chemical Engineering, University College London, London WC1E 7JE, UK

ARTICLE INFO

Article history:
Received 27 November 2017
Revised 8 January 2018
Accepted 29 January 2018

Keywords:
Pt/Beta
n-pentane isomerization
Zeolite particle size
Internal grain boundaries
Polycrystalline zeolite
Single-crystalline zeolite

ABSTRACT

The impact of particle size and internal grain boundaries of Beta zeolites was investigated in *n*-pentane isomerization over bifunctional Pt/Beta catalysts, by comparing the catalytic performance of four as-synthesized Pt/Beta samples that possess an identical Pt loading (0.5 wt%), but use four distinct Beta zeolites. Three of them contain polycrystalline zeolites, consisting of nano-sized crystals with a similar size of 9–13 nm, but having different average particle sizes (i.e., 1340, 830, and 250 nm) and numerous internal grain boundaries, as found via high-resolution transmission electron microscopy. The last catalyst contains single-crystalline zeolite, with an average particle size of 225 nm, and no observed internal grain boundaries. At low reaction temperature (<578 K), the particle size and internal grain boundaries do not change the apparent activity, because activity is controlled by reaction on the acid sites of the zeolite. At high reaction temperature (>614 K), a large particle size and the presence of internal grain boundaries significantly reduce the apparent activity, because of the extended diffusion path and additional diffusion barriers, which are probably caused by a mismatch in micropore alignment and gas-zeolite interfaces at these grain boundaries. Due to the small particle size and absence of internal grain boundaries, the observed activity for single-crystalline Beta can be 60–212% higher than for polycrystalline counterparts, even though it possesses a much weaker intrinsic acidity. This shows, remarkably, that single-crystalline zeolites with less internal grain boundaries can achieve a much higher catalytic activity.

1. Introduction

Branched alkanes are becoming the most favorable gasoline component, due to their high octane number and environmental friendliness when comparing to olefins and aromatics [1–5]. Such branched alkanes can be produced through isomerization of *n*-alkanes, normally using bifunctional catalysts. Early commercial catalysts, including $AlCl_3$ and metal on aluminosilicates, are no longer used, due to their poor performance and adverse effects on the environment [3]. Pt/chlorinated Al_2O_3 is very sensitive towards impurities (especially water and sulfur) in the feed and, in addition, corrodes reactors, although this catalyst is very active and still employed in some commercial processes [1,6,7]. Pt/zeolite is free of the aforementioned problems and, thus, has become the predominant catalyst for isomerization of *n*-alkanes [1,7].

The mechanism of *n*-alkanes isomerization over Pt/zeolites is typically described by the bifunctional model originally proposed by Weisz [8] and Coonradt and Garwood [9]. The *n*-alkanes are dehydrogenated into alkenes on Pt sites; subsequently, the alkenes are protonated on acid sites to yield alkylcarbenium ions that undergo C—C bond rearrangement and/or β-scission followed by de-protonation, yielding alkenes; finally, the product alkenes are hydrogenated on Pt sites, yielding branched alkanes [10,11]. The presence of Pt sites allows the protonation of alkenes, rather than the direct protonation of *n*-alkanes that is much more energetically unfavorable [12]. Besides, under hydrogen atmosphere, Pt sites are able to hydrogenate coke precursors, thus maintaining the stability of Pt/zeolites [13,14]. However, numerous studies [15–18] have confirmed that the C—C bond rearrangement on acid sites is the rate determining step in this reaction scheme if the Pt loading is high enough. The rate of C—C bond rearrangement is believed to be determined by the strength of Brønsted acid sites (BAS), which can be rigorously described by deprotonation energies [19,20]. Apart from the strength of BAS, the accessibility of BAS also significantly influences the apparent activity of Pt/zeolites and the

* Corresponding authors.
E-mail addresses: xgzhou@ecust.edu.cn (X. Zhou), m.coppens@ucl.ac.uk (M.-O. Coppens).

https://doi.org/10.1016/j.jcat.2018.01.033
0021-9517/

product distribution, due to the very strong diffusion limitations caused by the microporous (poresless than 2 nm in diameter) structure of zeolites. Therefore, designing the multiscale structure of zeolite-based catalysts is an effective way to improve this type of catalyst for the isomerization of *n*-alkanes.

Zeolite particle size influences the diffusion length of reacting molecules. Smaller zeolite crystals have larger effectiveness factors, corresponding to a higher utilization of their acid sites. To achieve better catalytic performance of zeolites, much effort has been devoted to shrinking their particle size and to introducing auxiliary mesoporosity, resulting in numerous synthesis protocols to manipulate such physical structures of zeolites [21–24]. However, most efforts overlook the fact that smaller zeolite size might, surprisingly, not lead to better catalytic performance for certain reactions. For example, Bonetto et al. [25] found that Beta zeolite with an average particle size of 0.40 μm performed best for oil cracking when comprehensively considering activity, selectivity, and stability. More recently, Jang et al. [26] reached a similar conclusion for methanol-to-olefin reactions using SAPO-34 and ZSM-5: a moderate particle size of 0.2–0.5 μm exhibited the best catalytic performance. They explained that smaller SAPO-34 particles deactivated quickly, due to pore blocking by coke, and smaller ZSM-5 particles did not deactivate rapidly but showed low activity due to a reduced number of Brønsted acid sites. More importantly, the change of zeolite particle size is often accompanied by the change of other structural parameters, such as the intercrystalline pore size distribution, and acidity; meanwhile, reaction temperature plays an important role in affecting the coupled diffusion-reaction process in zeolites. These factors may complicate the effects of zeolite particle size on the catalytic performance of Pt/zeolites for *n*-alkanes isomerization, especially at different reaction temperatures, and these effects have not been reported in the literature, to the best of our knowledge.

Internal grain boundaries exert a strong influence on mass transfer in zeolite particles. Due to aggregation and intergrowth of crystals, mismatch in structure and pore alignment are likely to occur where crystal grains meet, and internal defects or a disordered phase may also exist between the crystal grains [27–31]. Such imperfections within zeolite particles constitute internal grain boundaries, and can act as permeable barriers when transporting molecules. Vasenkov et al. [27,28] studied the diffusion of n-butane in silicalite and methane in ZSM-5 by using PFG NMR and Monte Carlo simulations, and suggested the existence of internal transport barriers caused by grain boundaries. Newsome and Sholl [29] simulated the diffusion of CH_4 and CF_4 in twinned silicalite (pure Si form of ZSM-5) using the dual control volume grand canonical molecular dynamics method, and further proved the existence of significant grain boundary resistances. Karwacki et al. [30] probed the source of internal transport barriers in ZSM-5 by combining spectroscopy, scattering and microscopy, and found that these barriers originate not only from a 90° mismatch in pore alignment, but also from small angle differences of only 0.5–2°. Besides, the gas-zeolite interfaces at the internal defects (voids) could be another source of internal transport barriers, according to numerous studies on surface barriers at external zeolite surfaces. These transport barriers could originate from blocked pore entrances, lattice defects, and mean-field differences, which have been investigated by using zero length chromatography [32,33], interference microscopy [34,35], fast time-resolved IR spectroscopy [36,37], frequency response [38,39], and molecular simulations [40–42]. Recently, Rao et al. [43] found that the catalytic performance of ZSM-5 for alkylation of benzene with ethylene may be limited by surface barriers at the external surface of the ZSM-5 crystals. However, how internal grain boundaries affect the catalytic performance of zeolites has not been studied in the literature up to now.

Pt/Beta was reported to be more active and selective than the commercial Pt/mordenite in catalyzing the isomerization of *n*-alkanes [1,3,7,15,44,45], raising the potential interest of this catalyst for industrial use. Meanwhile, *n*-pentane is the main component of Light Straight Run gasoline [3], and isomerization of *n*-pentane results in a significant octane number (RON) increase from 61.7 to 92.3. Therefore, it is of great industrial significance to study the effects of zeolite particle size and internal grain boundaries on *n*-pentane isomerization over Pt/Beta.

In this work, we prepared three Pt/Beta samples with polycrystalline Beta zeolites of different particle sizes (i.e., 1340, 830, and 250 nm) and, also, a sample with a single-crystalline Beta zeolite (225 nm). Their structure, texture, morphology, and acidity were characterized by XRD, SEM, HRTEM, N_2 sorption, ICP-AES, NH_3-TPD, and Py-IR. Finally, by comparing their catalytic performance for *n*-pentane isomerization, the effects of zeolite particle size and internal grain boundaries were determined.

2. Experimental

2.1. Catalyst preparation

2.1.1. Polycrystalline Beta zeolite synthesis

Polycrystalline Beta zeolites were synthesized by the hydrothermal method. Appropriate amounts of sodium hydroxide (≥96.0 wt%, Sinopharm Chemical Reagent Co., Ltd.), deionized water, tetraethylammonium hydroxide (TEAOH) (25 wt% in aqueous solution, Shanghai Cainorise Chemicals Co., Ltd.), and silica (34 wt% in aqueous solution, Sigma-Aldrich) were mixed and stirred with a magnetic stirrer until the solution was clear. Then, the dissolved sodium aluminate ($Al_2O_3 \geq 41$ wt%, Sinopharm Chemical Reagent Co., Ltd.) was dropwise added into the solution and stirred for 3 h. The molecular composition of the final mixture was $1SiO_2$:0.266TEAOH:0.106NaOH:$0.025Al_2O_3$:$11.8H_2O$, and this mixture was hydrothermally treated in a Teflon-lined stainless steel autoclave. The hydrothermal conditions (temperature and time) were adjusted to obtain polycrystalline Beta zeolites of different particle sizes, as shown in Table 1. After the hydrothermal treatment, the product was washed with deionized water and centrifuged repeatedly for three times, and then dried at 353 K for 8 h. Finally, to remove the organic template, the product was calcined in air at 823 K for 6 h with a temperature ramp of 1.5 K/min.

The protonated form of the polycrystalline Beta zeolites was obtained through ion exchange of the calcined product with a solution of 1 M NH_4Cl at 353 K for 8 h, followed by centrifugation, drying at 353 K for 8 h, and calcination at 823 K for 4 h (temperature ramp 1.5 K/min). The as-synthesized polycrystalline Beta samples were labeled as Beta-P-1340, Beta-P-830, and Beta-P-250 according to their average particle sizes determined from their SEM images. The histograms of their particle size distributions are given in Fig. S1 in the Supplementary Materials.

2.1.2. Single-crystal Beta zeolite synthesis

A single-crystalline Beta sample, denoted as Beta-S-225, was also synthesized using the hydrothermal method. The synthetic process for this single-crystal sample was the same to the aforementioned one. However, the molecular composition of its starting synthesis gel was $1SiO_2$:0.36TEAOH:0.106NaOH:$0.01Al_2O_3$:$11.8H_2O$, the hydrothermal reaction temperature was 393 K, and this reaction was continued for 8 days, as seen in Table 1.

2.1.3. Platinum loading

The as-synthesized Beta samples were loaded with 0.5 wt% Pt by incipient wetness impregnation with a solution of H_2PtCl_6 (Sigma-Aldrich). Afterwards, the samples were aged for 12 h, dried

Table 1
Molecular composition of reaction mixture and hydrothermal conditions for preparing Beta zeolite samples.

BEA-type zeolite	Reagent		Molecular composition of reaction mixture	Temperature (K)	Time (days)
	Si	Al	SiO_2: TEAOH:NaOH:Al_2O_3:H_2O		
Beta-P-1340	Silica sol	$NaAlO_2$	1:0.266:0.106:0.025:11.8	393	10
Beta-P-830	Silica sol	$NaAlO_2$	1:0.266:0.106:0.025:11.8	413	4
Beta-P-250	Silica sol	$NaAlO_2$	1:0.266:0.106:0.025:11.8	393	3
Beta-S-225	Silica sol	$NaAlO_2$	1:0.36:0.106:0.01:11.8	393	8

at 353 K for 8 h, and calcined in air at 723 K for 3 h. Finally, these samples were reduced in H_2 flow at 723 K for 2 h. These samples, prepared for catalytic tests, were labeled as Pt/Beta-P-1340, Pt/Beta-P-830, Pt/Beta-P-250, and Pt/Beta-S-225, according to the organization and particle size of Beta zeolites. The Pt loading of these catalysts is sufficient to make dehydrogenation and hydrogenation reactions reach equilibrium [6,16]. Besides, these catalysts have similar Pt dispersions and Pt particle sizes, as shown in Fig. S2 and Table S1 in the Supplementary Materials. Thus, the effects of Pt sites can be ignored when comparing the catalytic performance of the four catalyst samples.

2.2. Catalyst characterization

X-ray diffraction (XRD) patterns were recorded using a D8 advance A25 diffractometer (Bruker, Germany) equipped with a Cu Kα radiation source, and the measurements were conducted in the range $3° < 2\theta < 50°$ at a rate of 1.2°/min. Scanning electron microscopy (SEM) images were taken using a NOVA Nano SEM450 microscope (FEI, USA) operating at 3 kV. High-resolution transmission electron microscopy (HRTEM) images were taken using a JEM 2100 instrument (JEOL, Japan) operating at 200 kV. N_2 adsorption and desorption measurements were performed at a temperature of 77 K using an ASAP 2020 instrument (Micromeritics, USA). Prior to the measurements, the samples were degassed at 1.33×10^{-3} Pa and 523 K for 6 h. The total pore volumes were determined from the N_2 adsorbed volume at $p/p^0 = 0.99$. The specific surface areas, micropore volumes, and pore size distributions were calculated using the Brunauer–Emmett–Teller (BET) method, t-plot, and Barrett–Joyner–Halenda (BJH) methods, respectively.

Chemical compositions of the as-synthesized catalysts were determined by inductively coupled plasma-atomic emission spectroscopy (ICP-AES), using an IRIS 1000 instrument (Thermal Elemental, USA). The temperature programmed desorption of ammonia (NH_3-TPD) was performed using an AutoChem II 2920 (Micromeritics, USA). Prior to desorption of ammonia, the samples were kept at 373 K in NH_3 flow (30 ml/min) for 40 min. The TPD profiles were determined when heating the samples from 373 to 973 K at a temperature ramp of 15 K/min in He flow (30 ml/min). Infrared spectra of pyridine adsorption (Py-IR) on Beta zeolites were recorded on a Tensor 27 spectrometer (Bruker, Germany) at 473 K and 673 K. The amount of pyridine adsorbed on Brønsted (Py-H^+) and Lewis (Py-L) acid sites [46] was calculated from integrating the band at 1545 and 1454 cm^{-1}, respectively. CO chemisorption was measured on an AutoChem 2920 instrument (Micromeritics, USA) at 318 K to determine Pt dispersions of the catalyst samples.

2.3. Catalytic tests

The *n*-pentane isomerization reaction was performed in a fixed-bed reactor under H_2 at atmospheric pressure and different temperatures, i.e., 578, 614, and 653 K. The fixed-bed reactor was equipped with a quartz tube with an inner diameter of 6 mm; 0.03 g catalyst powder was well dispersed in 0.16 g silica sand and then this mixture was loaded into the quartz tube. Prior to the reaction, the catalyst was reduced in H_2 flow at 723 K for 2 h and subsequently cooled down to the reaction temperature under H_2 flow. Then, *n*-pentane was fed into the reactor by bubbling H_2 in a saturator loaded with liquid *n*-pentane and maintained at 273 K, yielding a flow of binary mixture with a *n*-pentane partial pressure of 0.26 atm and weight hourly space velocity (WHSV) of *n*-pentane of 14 h^{-1}. Meanwhile, another flow of H_2 was added to maintain a H_2/*n*-pentane molar ratio of 4.8. The product gas mixture was analyzed by an on-line gas chromatograph (FuLi GC9790, China), equipped with a flame ionization detector (FID) and a HP-PONA capillary column (50 m × 0.2 mm × 0.5 μm).

3. Results and discussion

3.1. Structure, morphology, and texture

The structural, morphological, and textural properties of the four as-synthesized Beta samples were determined by XRD, SEM, HRTEM, and N_2 adsorption and desorption measurements. Their main features are summarized in Table 2.

The XRD patterns of the four Beta samples are compared in Fig. 1. All these patterns display characteristic peaks at $2\theta = 7.8°$, 13.4°, 21.5°, 22.6°, 25.4°, 27.0°, and 29.7°, attributed to the typical Beta phase with a BEA-type structure [47]. Besides, these patterns show high peak intensities and low background scattering, indicating that each sample is highly crystalline. The crystallite sizes of Beta-P-1340, Beta-P-830, and Beta-P-250 are estimated to be 11.2, 10.1, and 9.5 nm, respectively, according to the Scherrer equation [48]:

$$d = \frac{0.9\lambda}{w\cos\theta} \quad (1)$$

where d is the crystallite size in nm, λ is the radiation wavelength (0.154 nm), θ is the diffraction peak angle, and w is the line width of the XRD peak at half-peak intensity. Since the Scherrer equation may not be accurate when a crystal size is larger than 100 nm, due to crystal microstrains [49], the crystal size of Beta-S-225 is determined by combining SEM, HRTEM and SAED, as discussed further on.

The SEM images, Fig. 2a-c, show that Beta-P-1340, Beta-P-830, and Beta-P-250 all have very coarse external surfaces and ill-defined (irregular) external shapes, implying that the three samples are polycrystalline, rather than single-crystalline. Thus, such Beta zeolites are inferred to be aggregates of nano-sized crystals with an average size of 9–12 nm, based on the crystal sizes determined from XRD patterns. Besides, these Beta zeolites display different average particle sizes (1340, 830, and 250 nm for Beta-P-1340, Beta-P-830, and Beta-P-250), and their histograms of particle size distribution are given in Fig. S1a–c of the Supplementary Materials. Fig. 2d shows that Beta-S-225, in contrast, exhibits a comparatively smooth external surface and well-faceted morphology, implying a single-crystalline nature of this Beta sample. The average crystal size of Beta-S-225 is 225 nm, and the histogram

Table 2
Characteristics of the Beta zeolites synthesized in the present work.

Properties	Unit	Beta-P-1340	Beta-P-830	Beta-P-250	Beta-S-225
Si/Al ratio[a]		20	23	20	34
Crystal size obtained from XRD	nm	11.2	10.1	9.5	Not available
Crystal size obtained from TEM	nm	12.7	12.3	11.6	225
Particle size[b]	nm	1340	830	250	225
S_{BET}[c]	m^2/g	578	587	631	525
S_{ext}[d]	m^2/g	251	249	259	95
V_{total}[e]	cm^3/g	0.36	0.36	0.53	0.35
V_{micro}[f]	cm^3/g	0.16	0.16	0.18	0.20
Py-H^+(473 K)[g]	mmol/g	0.187	0.165	0.192	0.064
Py-L(473 K)[h]	mmol/g	0.148	0.125	0.156	0.060
Py-H^+(673 K)[i]	mmol/g	0.115	0.138	0.124	0.020
Py-L(673 K)[j]	mmol/g	0.140	0.056	0.122	0.077

[a] Si/Al molar ratio measured by using ICP-AES.
[b] Average particle size determined from SEM.
[c] Specific surface area calculated by BET method.
[d] External surface area calculated by t-plot method.
[e] Total volume determined from the adsorbed volume at $p/p^0 = 0.99$.
[f] Micropore volume calculated by t-plot method.
[g,h,i,j] Brønsted (Py-H^+) and Lewis (Py-L) acid sites content calculated from Py-IR (473 and 673 K).

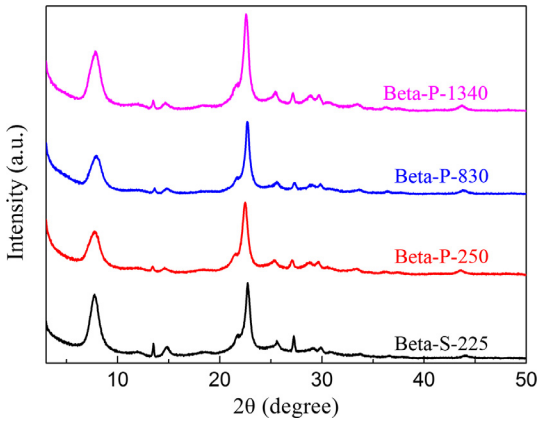

Fig. 1. Wide-angle powder XRD patterns of the as-synthesized Beta samples.

of its crystal size distribution is displayed in Fig. S1d in the Supplementary Materials.

The HRTEM images, Fig. 3a-c, show that the particle peripheries of Beta-P-1340, Beta-P-830, and Beta-P-250 consist of nano-sized crystals with an average size of 11–13 nm, which provides direct proof that these three samples are polycrystalline. Their SAED images inserted in Fig. 3a–c display diffraction rings, further confirming the polycrystalline nature of these Beta zeolites. For polycrystalline zeolites, there are internal grain boundaries where defects, disordered phases, or a mismatch in micropore alignment are present. In terms of Beta-P-1340 and Beta-P-830, the small crystals are closely packed, leaving almost no mesoporosity in these particles; therefore, a mismatch in micropore alignment, which can be deduced from the inconsistent orientations of lattice fringes [30], could be a predominant source of internal grain boundaries. With regards to Beta-P-250, there is some mesoporosity in the particle, which can be indicated by the bright contrasts, so that both defects and mismatched alignment would occur on its internal grain boundaries. Fig. 3d shows that Beta-S-225 possesses ordered lattice fringes and a SAED pattern with bright spots, which evidences the single-crystalline nature of Beta-S-225.

N_2 adsorption and desorption isotherms in Fig. 4 show the textural properties of the four Beta samples, and their BET surface area (S_{BET}), external surface area (S_{ext}), total pore volume (V_{total}), and micropore volume (V_{micro}) are collected in Table 2. All the samples display a steep uptake at very low partial pressure, confirming the presence of much microporosity. Beta-P-1340 and Beta-S-225 show a Type I isotherm, according to the IUPAC classification, which is indicative of typical microporous zeolites without mesoporosity. Beta-P-1340 shows a slight but continuous rise of the adsorbed amount after the fast uptake at low partial pressure, because of its coarse external surface (see Fig. 2a) and large external surface area (251 m^2/g), while the isotherms of Beta-S-225 reach a plateau, due to its relatively smooth external surface (see Fig. 2d) and small external surface area (95.1 m^2/g). Beta-P-830 and Beta-P-250 exhibit a combination of Type I isotherm and H4 hysteresis loop, which is characterized by a step-down at a relative pressure p/p_0 of 0.47. This type of hysteresis loop indicates that the two Beta samples contain some mesopores that are accessible only via micropores and are not directly connected to the external surface [50,51]. It is worth noting that the micropore volumes of the four Beta samples are slightly different (see Table 2), which may be due to their different crystallinities and properties of the internal grain boundaries.

In summary, the three polycrystalline Beta samples (Beta-P-1340, Beta-P-830, and Beta-P-250) consist of nano-sized crystals of similar size (9–13 nm) that are aggregated into particles of different sizes (250–1340 nm). In such polycrystalline samples, there are a lot of internal grain boundaries. For Beta-P-1340 and Beta-P-830, mismatch in micropore alignment is probably predominant on the internal grain boundaries; for Beta-P-250, both defects and mismatch would be present. Beta-S-225 is a single-crystalline zeolite with an average crystal size of 225 nm; no internal grain boundaries are observed via the above characterization methods, although their complete absence cannot be excluded.

3.2. Acidity

The acidic properties of the four Beta samples were characterized by ICP-AES, NH_3-TPD, and Py-IR; these properties are summarized in Table 2. The Si/Al molar ratios of the three polycrystalline samples, measured by ICP-AES, are close (Si/Al = 20–23); the one of the single-crystalline sample is much higher (Si/Al = 34), which implies that the acidity of Beta-S-225 can be significantly different from that of Beta-P-1340, Beta-P-830, and Beta-P-250. In addition, the acidities of these polycrystalline samples may also be different because of their possibly distinct Al distributions, although they have similar Si/Al ratios. It is worth mentioning that a zeolite with high Si/Al ratio tends to be large in crystal size [52,53], which is consistent with the observations in this work.

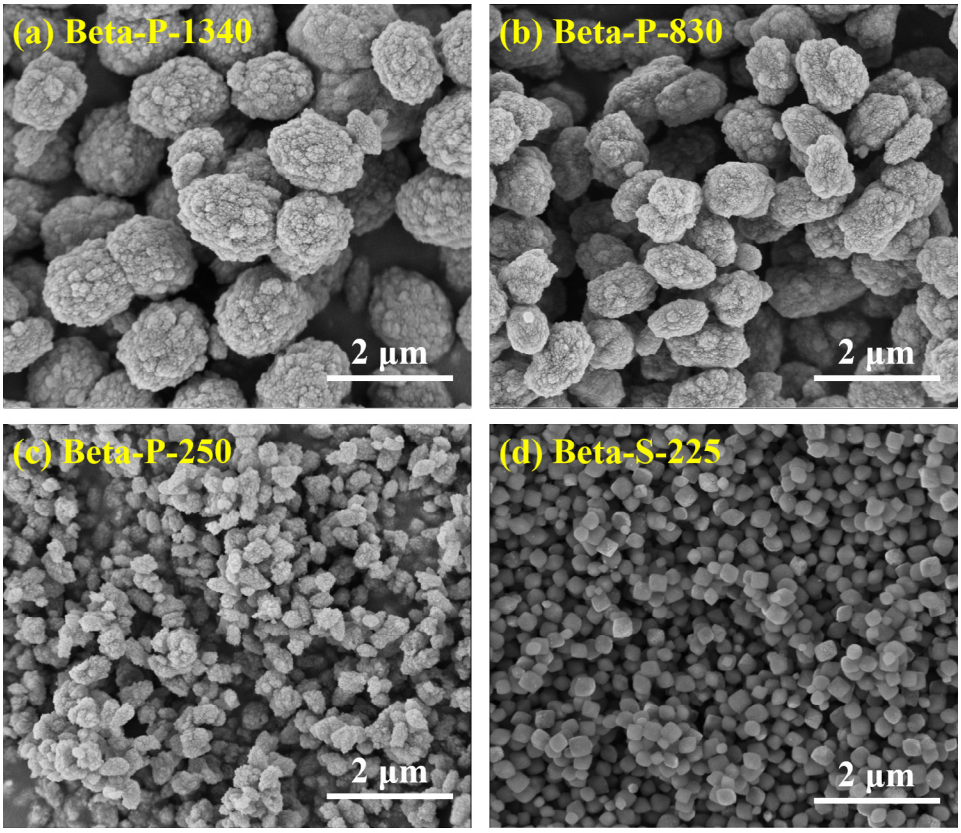

Fig. 2. Representative SEM images of (a) Beta-P-1340, (b) Beta-P-830, (c) Beta-P-250, and (d) Beta-S-225.

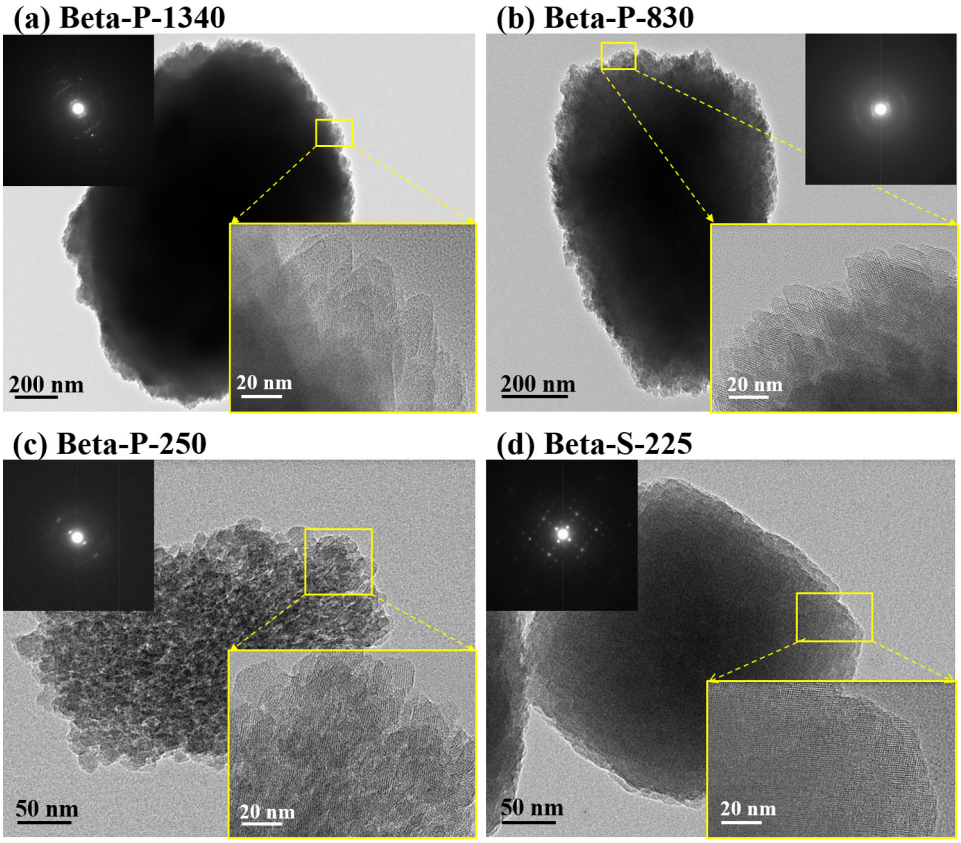

Fig. 3. Representative TEM images of (a) Beta-P-1340, (b) Beta-P-830, (c) Beta-P-250, and (d) Beta-S-225. The inserts with a yellow frame are TEM images taken at the particle peripheries; the inserts with a black background are the SAED patterns.

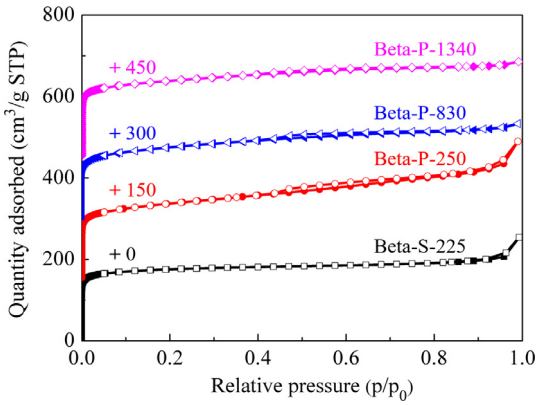

Fig. 4. N_2 adsorption (solid symbols) and desorption (open symbols) isotherms at 77 K of the Beta samples.

All the NH_3-TPD profiles (see Fig. 5) are composed of two desorption peaks, one at low temperature and the other at high temperature. The desorption temperature reflects the strength of the acid sites, while the peak area corresponds to the number of acid sites. Obviously, Beta-S-225 has much fewer weak or strong acid sites than Beta-P-1340, Beta-P-830, and Beta-P-250, and the three polycrystalline samples only have slight differences in acidity, because of their similar Si/Al ratios.

Pyridine-adsorption IR spectra (Py-IR) at 473 K and 673 K (see Fig. 6) provide more detailed information on the acidic properties. All the Beta samples display bands at 1545 and 1454 cm^{-1} attributed to Brønsted acid sites (BAS) and Lewis acid sites (LAS) [46], and the band at 1490 cm^{-1} corresponds to the interaction of pyridine with both BAS and LAS [54]. The amounts of BAS and LAS are summarized in Table 2. The total number of BAS (measured at 473 K) follows a decreasing order in Beta-P-250 ≈ Beta-P-1340 > Beta-P-830 ≫ Beta-S-225; the number of strong BAS (measured at 673 K) shows a decreasing trend in Beta-P-830 > Beta-P-250 > Beta-P-1340 ≫ Beta-S-225. In summary, the three polycrystalline Beta samples have a similar number of BAS, although slight differences still exist; the single-crystalline sample possesses much less BAS. BAS are believed to be crucial active sites for *n*-alkanes isomerization, and, more importantly, the number of BAS can be even directly correlated with the isomerization activity [6,55,56]. Thus, these acidic properties can determine the catalytic performance of Pt/Beta samples, if mass transfer resistance is negligible.

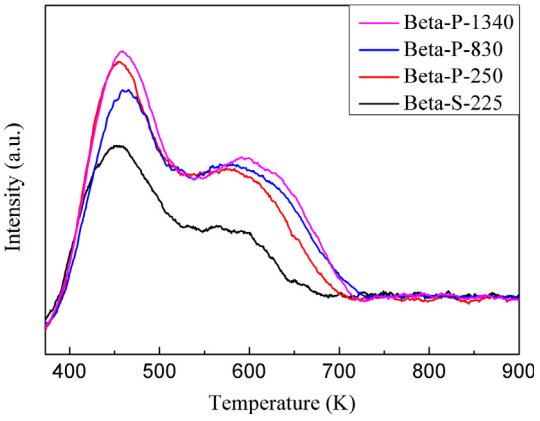

Fig. 5. NH_3-TPD profiles (normalized by the sample mass) of the Beta samples.

3.3. Catalytic performance

Pt/Beta-P-1340, Pt/Beta-P-830, Pt/Beta-P-250, and Pt/Beta-S-225 were tested as catalysts for *n*-pentane isomerization at 578, 614, and 653 K under atmospheric pressure. The variation of product (*i*-pentane) selectivity with time-on-steam is shown in Fig. S3 in the Supplementary Materials; the variation of *n*-pentane conversion with time-on-stream is presented in Fig. 7. All the catalyst samples show an excellent *i*-pentane selectivity (>96%), which remains almost unchanged with reaction time, as seen in Fig. S3. However, the conversion decreases with time-on-stream, probably because of coke deposition on acid sites, especially the strong ones [4,6], as shown in Fig. 7.

The conversion on a catalyst sample is strongly affected by its zeolite particle size and internal grain boundaries in *n*-pentane isomerization over Pt/Beta, which will be separately analysed and discussed in Sections 3.1 and 3.3.2 by comparing the catalytic performance of the four Pt/Beta samples.

3.3.1. Effects of particle size

To obtain the effects of zeolite particle size, the conversions on Pt/Beta-P-1340, Pt/Beta-P-830, and Pt/Beta-P-250 are first compared, as these catalysts possess Beta zeolites with similar texture and acidity, but different particle sizes (250–1340 nm). These three catalysts display very close conversions at a low reaction temperature of 578 K (see Fig. 7a), while their conversions exhibit a decreasing trend in Pt/Beta-P-250 > Pt/Beta-P-830 > Pt/Beta-P-1340 at reaction temperatures of 614 and 653 K (see Fig. 7b and c). To compare the catalytic activity on the same basis, the turnover frequencies (TOFs) for *n*-pentane isomerization at the initial measuring time (t = 0.5 h), based on the total number of BAS (Py-H^+(473 K), see Table 2), as both strong and weak BAS can catalyze *n*-pentane isomerization, were calculated and summarized in

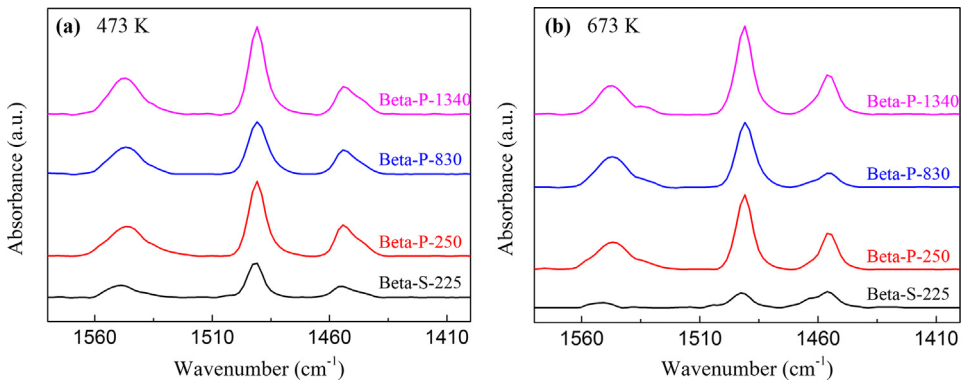

Fig. 6. IR spectra (normalized by the sample mass) of pyridine adsorbed on the Beta samples at (a) 473 K and (b) 673 K.

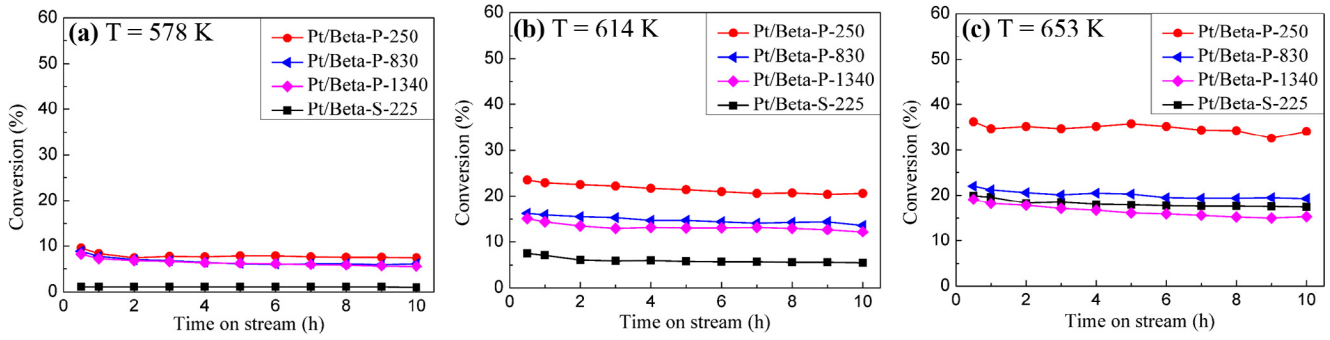

Fig. 7. Conversion of *n*-pentane versus time on stream over Pt/Beta-P-1340, Pt/Beta-P-830, Pt/Beta-P-250, and Pt/Beta-S-225, for (a) T = 578 K, (b) T = 614 K, and (c) T = 653 K. The other reaction conditions are as follows: P = 1 atm, WHSV = 14 h^{-1}, H_2/*n*-pentane molar ratio = 4.8.

Table 3
TOFs for *n*-pentane isomerization over the four catalyst samples at the earliest measuring time (t = 0.5 h) and their approximate, average activation energies estimated from Arrhenius plots over a reaction temperature range from 578 K to 653 K.

Catalysts	TOF (s^{-1})			E_a (kJ/mol)
	578 K	614 K	653 K	
Pt/Beta-P-1340	0.33	0.59	0.74	34.0
Pt/Beta-P-830	0.40	0.73	1.00	38.7
Pt/Beta-P-250	0.38	0.93	1.44	55.7
Pt/Beta-S-225	0.13	0.87	2.31	121.5

Table 3, since the *n*-pentane isomerization activity can be directly correlated to the number of BAS [6]. At 578 K, the TOFs for the three catalysts are very close; however, at 614 and 653 K, these TOFs show remarkable differences and follow the same decreasing order in Pt/Beta-P-250 > Pt/Beta-P-830 > Pt/Beta-P-1340.

At low reaction temperature (578 K), the apparent reaction rate is probably controlled by reaction on the acid sites, hence, the amount and strength of the acid sites determines the conversion. Pt/Beta-P-1340, Pt/Beta-P-830, and Pt/Beta-P-250 possess similar acidity, resulting in close conversions and TOFs; the slight differences in TOFs for the three catalysts are mainly because of the small differences in the proportion of strong acid sites that are more active in catalyzing *n*-pentane isomerization. At high reaction temperatures (614 and 653 K), mass transfer limitations affect the apparent reaction rate. A larger particle size leads to longer diffusion paths and stronger diffusion limitations, leading to a lower apparent reaction rate, as reflected by the lower conversion and TOF in this work.

To confirm the strong influence of mass transfer, the apparent activation energy was calculated. Values are listed in Table 3. The apparent activation energy decreases with the increase in zeolite particle size, and these activation energies are much lower than the one (124 kJ/mol) measured by Matsuda et al. [57] at low reaction temperature (<578 K), where the apparent reaction rate is controlled by reaction. This observation suggests that the apparent reaction rate is limited by mass transfer, as a strongly reduced apparent activation energy on otherwise similar samples reflects increased mass transfer limitations [58]. In Table 3, only three data points are used to determine an apparent activation energy, which may not be very accurate, but should be adequate to observe qualitative changes in activation energy. From these measurements, the apparent activation energy for Pt/Beta-P-1340 (34.0 kJ/mol) is close to the one for Pt/Beta-P-830 (38.7 kJ/mol), as the two Beta samples have close morphology and texture (see Section 3.1), and there is good agreement with the activation energy measured by Matsuda et al. [57] for the single-crystalline sample, Pt/Beta-S-225. These results lend credibility to the activation energies.

3.3.2. Effects of internal grain boundaries

To demonstrate the effects of internal grain boundaries, the conversions and TOFs of Pt/Beta-P-250 and Pt/Beta-S-225 are compared, as the two catalysts have similar particle sizes, but different internal structures. For Pt/Beta-P-250, there are numerous internal grain boundaries, while, for Pt/Beta-S-225, no internal grain boundaries are observed in this work. The conversion for Pt/Beta-S-225 is smaller than the one for Pt/Beta-P-250 (see Fig. 7), because of its much smaller number of acid sites. The TOF in Table 3 gives the apparent reaction rate per BAS. At 578 K, the TOF for Pt/Beta-S-225 is smaller than the one for Pt/Beta-P-250; at 614 K, the TOF approaches its counterpart; at 653 K, this TOF is 60% higher.

Pt/Beta-S-225 has a lower proportion of strong BAS (31.3%) than Pt/Beta-P-250 (64.6%), probably resulting in the lower TOF at 578 K, where the apparent reaction rate is controlled by chemical reaction. At 614 K, the apparent reaction rate for Pt/Beta-P-250 is significantly affected by mass transfer, but the one for Pt/Beta-S-225 is still controlled by reaction, as evidenced by the activation energy in Table 3. The two catalyst samples are similar in zeolite particle size, thus the significant increase in mass transfer limitations can be attributed to the numerous internal grain boundaries in Pt/Beta-P-250. At the internal grain boundaries, the mismatch in micropore alignment and the gas-zeolite interfaces in the isolated defects can create additional diffusion barriers [27–30], which explains the strong mass transfer limitations in Pt/Beta-P-250. At 653 K, the mass transfer limitations in Pt/Beta-P-250 are even stronger, resulting in a 60% higher TOF for Pt/Beta-S-225. The apparent activation energy for Pt/Beta-P-250 (55.7 kJ/mol) is much smaller than the one for Pt/Beta-S-225 (121.5 kJ/mol), providing further evidence for the strong diffusion barriers caused by the presence of internal grain boundaries. If Pt/Beta-S-225 had a similar amount and strength of acid sites as Pt/Beta-P-250, it should be even more active.

Finally, it should be noted that the apparent TOF of Pt/Beta-S-225 is 131% and 212% higher than the TOFs of Pt/Beta-P-830 and Pt/Beta-P-1340, respectively, which are affected by both zeolite particle size and internal grain boundaries. Therefore, the preferred zeolite should not only be small in size, but also single-crystalline in nature, minimizing internal grain boundaries.

4. Conclusions

In this work, the effects of zeolite particle size and internal grain boundaries were probed in *n*-pentane isomerization over as-synthesized Pt/Beta catalysts with different Beta zeolite morphologies. Three polycrystalline and one single-crystalline Beta zeolite samples were prepared by the hydrothermal method. The polycrystalline ones possess similar acidic properties, but different particle sizes (250–1340 nm), and they also contain numerous

internal grain boundaries. The single-crystalline one has a particle size of 225 nm, and, in contrast, it shows no observable internal grain boundaries.

At low reaction temperature (<578 K), the isomerization activity is controlled by the chemical reactions on the active, acid sites, thus determined by the acidic properties of Beta zeolites; therefore, neither zeolite particle size nor internal grain boundaries change the apparent activity. At high reaction temperature (>614 K), the isomerization activity is strongly affected by mass transfer, as demonstrated by greatly reduced apparent activation energies (34.0–55.7 kJ/mol) compared to the one reported in the literature (124 kJ/mol) [57]. A large particle size leads to extended diffusion paths, while, at the grain boundaries, mismatch in pore alignment and gas-zeolite interfaces in isolated mesopores may cause diffusion barriers. Therefore, the isomerization activity increases with decreased zeolite particle size and the absence of internal grain boundaries. The TOF of the single-crystalline Beta zeolite is 60–212% higher than the ones of the polycrystalline samples at 653 K, even though its acidity is much weaker.

These results suggest that not only effects of particle size, but also, most importantly, internal grain boundaries, must be accounted for when designing and synthesizing zeolitic materials for catalysis.

Acknowledgements

This work was supported by the National Natural Science Foundation of China (21706067 and 91434117), the China Postdoctoral Science Foundation (2016M600289) and the Fundamental Research Funds for the Central Universities (222201714004 and 222201718003). M.-O.C is supported by the EPSRC "Frontier Engineering" Centre for Nature Inspired Engineering (EP/K038656/1) and the UK Catalysis Hub (EP/K014706/1).

Appendix A. Supplementary material

Supplementary data associated with this article can be found, in the online version, at https://doi.org/10.1016/j.jcat.2018.01.033.

References

[1] A. Chica, A. Corma, J. Catal. 187 (1999) 167.
[2] A. Chica, A. Corma, P.J. Miguel, Catal. Today 65 (2001) 101.
[3] C.M. López, V. Sazo, P. Pérez, L.V. García, Appl. Catal. A Gen. 372 (2010) 108.
[4] H.D. Setiabudi, A.A. Jalil, S. Triwahyono, N.H.N. Kamarudin, R. Jusoh, Chem. Eng. J. 217 (2013) 300.
[5] V.M. Akhmedov, S.H. Al-Khowaiter, Catal. Rev. 49 (2007) 33.
[6] C. Woltz, Kinetic studies on alkane hydroisomerization over bifunctional catalysts, Technische Universität München, 2005.
[7] Z.B. Wang, A. Kamo, T. Yoneda, T. Komatsu, T. Yashima, Appl. Catal. A Gen. 159 (1997) 119.
[8] P.B. Weisz, Adv. Catal. 13 (1962) 137.
[9] H.L. Coonradt, W.E. Garwood, Ind. Eng. Chem. Process Des. Dev. 3 (1964) 38.
[10] E. Blomsma, J.A. Martens, P.A. Jacobs, J. Catal. 159 (1996) 323.
[11] E. Blomsma, J.A. Martens, P.A. Jacobs, J. Catal. 165 (1997) 241.
[12] P.A. Jacobs, J.A. Martens, Stud. Surf. Sci. Catal. 58 (1991) 445.
[13] N.M. Rodriguez, P.E. Anderson, A. Wootsch, U. Wild, R. Schlögl, Z. Paal, J. Catal. 197 (2001) 365.
[14] N. Essayem, Y.B. Taârit, C. Feche, P.Y. Gayraud, G. Sapaly, C. Naccache, J. Catal. 219 (2003) 97.
[15] T. Yashima, Z.B. Wang, A. Kamo, T. Yoneda, T. Komatsu, Catal. Today. 29 (1996) 279.
[16] A. Brito, F.J. García, M.C. Alvarez-Galván, M.E. Borges, C. Díaz, V.A. de la Peña O'Shea, Catal. Commun. 8 (2007) 2081.
[17] R. Ravishankar, S. Sivasanker, Appl. Catal. A Gen. 142 (1996) 47.
[18] F. Alvarez, F.R. Ribeiro, G. Perot, C. Thomazeau, M. Guisnet, J. Catal. 162 (1996) 179.
[19] J. Macht, R.T. Carr, E. Iglesia, J. Catal. 264 (2009) 54.
[20] M. Boronat, P.M. Viruela, A. Corma, J. Am. Chem. Soc. 126 (2004) 3300.
[21] V. Valtchev, G. Majano, S. Mintova, J. Pérez-Ramírez, Chem. Soc. Rev. 42 (2013) 263.
[22] J. Perez-Ramírez, C.H. Christensen, K. Egeblad, C.H. Christensen, J.C. Groen, Chem. Soc. Rev. 37 (2008) 2530.
[23] W. Schwieger, A.G. Machoke, T. Weissenberger, A. Inayat, T. Selvam, M. Klumpp, A. Inayat, Chem. Soc. Rev. 45 (2016) 3353.
[24] W.J. Roth, P. Nachtigall, R.E. Morris, J. Cejka, Chem. Rev. 114 (2014) 4807.
[25] L. Bonetto, M.A. Camblor, A. Corma, J. Pérez-Pariente, Appl. Catal. A Gen. 82 (1992) 37.
[26] H.G. Jang, H.K. Min, J.K. Lee, S.B. Hong, G. Seo, Appl. Catal. A Gen. 437 (2012) 120.
[27] S. Vasenkov, W. Böhlmann, P. Galvosas, O. Geier, H. Liu, J. Kärger, J. Phys. Chem. B 105 (2001) 5922.
[28] S. Vasenkov, J. Kärger, Micropor. Mesopor. Mater. 55 (2002) 139.
[29] D. Newsome, D.S. Sholl, J. Phys. Chem. B 110 (2006) 22681.
[30] L. Karwacki, M.H.F. Kox, D.A. Matthijs de Winter, M.R. Drury, J.D. Meeldijk, E. Stavitski, W. Schmidt, M. Mertens, P. Cubillas, N. John, A. Chan, N. Kahn, S.R. Bare, M. Anderson, J. Kornatowski, B.M. Weckhuysen, Nat. Mater. 8 (2009) 959.
[31] Z. Liu, T. Ohsuna, K. Sato, T. Mizuno, T. Kyotani, T. Nakane, O. Terasaki, Chem. Mater. 18 (2006) 922.
[32] A.R. Teixeira, C.C. Chang, T. Coogan, R. Kendall, W. Fan, P.J. Dauenhauer, J. Phys. Chem. C 117 (2013) 25545.
[33] C.C. Chang, A.R. Teixeira, C. Li, P.J. Dauenhauer, W. Fan, Langmuir 29 (2013) 13943.
[34] P. Kortunov, L. Heinke, S. Vasenkov, C. Chmelik, D.B. Shah, J. Kärger, R.A. Rakoczy, Y. Traa, J. Weitkamp, J. Phys. Chem. B 110 (2006) 23821.
[35] J.C. Saint Remi, A. Lauerer, C. Chmelik, I. Vandendael, H. Terryn, G.V. Baron, J.F. M. Denayer, J. Kärger, Nat. Mater. 15 (2016) 401.
[36] S.J. Reitmeier, R.R. Mukti, A. Jentys, J.A. Lercher, J. Phys. Chem. C 112 (2008) 2538.
[37] O.C. Gobin, S.J. Reitmeier, A. Jentys, J.A. Lercher, J. Phys. Chem. C 115 (2011) 1171.
[38] O.C. Gobin, S.J. Reitmeier, A. Jentys, J.A. Lercher, J. Phys. Chem. C 113 (2009) 20435.
[39] A.R. Teixeira, X. Qi, C.-C. Chang, W. Fan, W.C. Conner, P.J. Dauenhauer, J. Phys. Chem. C 118 (2014) 22166.
[40] N.E.R. Zimmermann, B. Smit, F.J. Keil, J. Phys. Chem. C 116 (2012) 18878.
[41] N.E.R. Zimmermann, T.J. Zabel, F.J. Keil, J. Phys. Chem. C 117 (2013) 7384.
[42] N.E.R. Zimmermann, B. Smit, F.J. Keil, J. Phys. Chem. C 114 (2010) 300.
[43] S.M. Rao, E. Saraci, R. Gläser, M.-O. Coppens, Chem. Eng. J. 329 (2017) 45.
[44] J. Lee, H. Rhee, Catal. Today 38 (1997) 235.
[45] K.J. Chao, H.C. Wu, L.J. Leu, Appl. Catal. A Gen. 143 (1996) 223.
[46] A. Astafan, M.A. Benghalem, Y. Pouilloux, J. Patarin, N. Bats, C. Bouchy, T.J. Daou, L. Pinard, J. Catal. 336 (2016) 1.
[47] F. Taborda, T. Willhammar, Z. Wang, C. Montes, X. Zou, Micropor. Mesopor. Mater. 143 (2011) 196.
[48] A.G. Popov, V.S. Pavlov, I.I. Ivanova, J. Catal. 335 (2016) 155.
[49] A.W. Burton, K. Ong, T. Rea, I.Y. Chan, Micropor. Mesopor. Mater. 117 (2009) 75.
[50] M. Thommes, B. Smarsly, M. Groenewolt, P.I. Ravikovitch, A.V. Neimark, Langmuir 22 (2006) 756.
[51] M. Thommes, K.A. Cychosz, Adsorption 20 (2014) 233.
[52] W.J. Kim, M.C. Lee, D.T. Hayhurst, Micropor. Mesopor. Mater. 26 (1998) 133.
[53] M.A. Camblor, A. Mifsud, J. Pérez-Pariente, Zeolites 11 (1991) 792.
[54] E.P. Parry, J. Catal. 2 (1963) 371.
[55] M. Guisnet, N.S. Gnep, Appl. Catal. A Gen. 146 (1996) 33.
[56] H.D. Setiabudi, A.A. Jalil, S. Triwahyono, J. Catal. 294 (2012) 128.
[57] T. Matsuda, K. Watanabe, H. Sakagami, N. Takahashi, Appl. Catal. A Gen. 242 (2003) 267.
[58] M. Höchtl, A. Jentys, H. Vinek, J. Catal. 190 (2000) 419.